

Article

Long-Range Mineral Dust Transport Events in Mediterranean Countries

Francesca Calastrini ^{1,2,*}, Gianni Messeri ^{1,2} and Andrea Orlandi ³ ¹ Istituto di BioEconomia IBE-CNR, 50145 Firenze, Italy; messeri@lamma.toscana.it or gianni.messeri@ibe.cnr.it² Consorzio LaMMA, Sesto Fiorentino, 50019 Firenze, Italy³ ENEA, SSPT-CLIMAR, 40121 Bologna, Italy; andrea.orlandi@enea.it

* Correspondence: calastrini@lamma.toscana.it or francesca.calastrini@ibe.cnr.it

Abstract: Mineral dust from desert areas accounts for a large portion of aerosols globally, estimated at 3–4 billion tons per year. Aerosols emitted from arid and semi-arid areas, e.g., from parched lakes or rivers, are transported over long distances and have effects on a global scale, affecting the planet's radiative balance, atmospheric chemistry, cloud formation and precipitation, marine biological processes, air quality, and human health. Desert dust transport takes place in the atmosphere as the result of a dynamical sequence beginning with dust uplift from desert areas, then followed by the long-range transport and terminating with the surface deposition of mineral dust in areas even very far from dust sources. The Mediterranean basin is characterized by frequent dust intrusion events, particularly affecting Spain, France, Italy, and Greece. Such events contribute to the increase in PM₁₀ and PM_{2.5} concentration values, causing legal threshold values to be exceeded. In recent years, these events have shown a non-negligible increase in frequency and intensity. The present work reports the results of an analysis of the dust events that in recent years (2018–2023) affected the Mediterranean area and in particular central Italy, focusing on the more recurrent meteorological configurations leading to long-range transport and on the consequent increase in aerosol concentration values. A method for desert intrusion episodes identification has been developed using both numerical forecast model data and PM₁₀ observed data. A multi-year dataset has been analyzed by applying such an identification method and the resulting set of dust events episodes, affecting central Italy, has been studied in order to highlight their frequency on a seasonal basis and their interannual variability. In addition, a first attempt at a meteorological classification of desert intrusions has been carried out to identify the most recurrent circulation patterns related to dust intrusions. Understanding their annual and seasonal variations in frequency and intensity is a key topic, whose relevance is steeply growing in the context of ongoing climate change.

Keywords: mineral desert dust; PM₁₀; weather types classification

Citation: Calastrini, F.; Messeri, G.; Orlandi, A. Long-Range Mineral Dust Transport Events in Mediterranean Countries. *Air* **2024**, *2*, 444–467. <https://doi.org/10.3390/air2040026>

Academic Editor: Angelo Riccio

Received: 31 October 2024

Revised: 5 December 2024

Accepted: 5 December 2024

Published: 12 December 2024



Copyright: © 2024 by the authors. Licensee MDPI, Basel, Switzerland. This article is an open access article distributed under the terms and conditions of the Creative Commons Attribution (CC BY) license (<https://creativecommons.org/licenses/by/4.0/>).

1. Introduction

Mineral desert dust constitutes a significant component of atmospheric aerosols on a global scale [1–4]. The phenomenon of desert dust in the atmosphere and oceans is linked to a range of physical processes, including cloud formation and precipitation [5–7]. These processes can influence radiative transfer, either directly or indirectly. Consequently, desert dust plays a role in the development of meteorological dynamics and in feedback mechanisms on a climatological scale [8–10]. Moreover, mineral dust exerts a significant influence on the biogeochemical processes of the Earth system, affecting both terrestrial and oceanic ecosystems [11,12].

The presence of desert dust in the atmosphere is linked to the establishment of a sequence of processes, which can be described as follows: atmospheric loading, long-range transport, and ground deposition.

The dust loading into the atmosphere requires uplift mechanisms, linked to the wind intensity in the lower layers and the turbulence induced by them in the boundary layer,

associated with the presence of sufficiently intense and deep convection to carry the dust to high altitudes. Extreme phenomena linked to these dynamics are sandstorms and haboobs, which produce the uplift of large quantities of dust from the ground, with major impacts in the directly affected areas [1,2].

The availability of significative quantities of dust on the ground is specific to certain regions of the globe, characterized by arid conditions, which provide the accumulation of dust and sediment. This can be observed in areas such as desiccated or ephemeral rivers and lakes, which contain clay, silt, and salts [1,2,13]. These conditions are strongly influenced by soil moisture, and in some source areas, by snow cover. They are also subject to seasonal variations and climatic trends.

The source areas that contribute most to the release of mineral dust into the atmosphere are predominantly located within the desert regions of the subtropics. The main one of them is the Saharan area and its surroundings [1,13–15]. Other important source areas are placed in Arabia, central Asia, southwestern United States, and Australia [1,2,13]. In addition, the high-latitude arid zones ($>50^\circ$ N and $>40^\circ$ S) constitute source areas capable of releasing minor but not insignificant amounts of dust, amounting to about 5% of the global budget [16,17]. In a climate change scenario, the importance and extent of the various source areas could change significantly.

The atmospheric loading phase is followed by the long-range transport phase: the dust plume formed in the first phase is transported by the intense high-altitude winds. The distance over which the dust is transported depends on the wind intensity, in some cases, far away from the source areas.

The recurring development of similar atmospheric circulation patterns is reflected in the regular occurrence of dust transport events from a given source area to certain deposition areas. On the other hand, on a given deposition area, dust can be transported originating from different source areas, depending on the recurrent onset of different circulation patterns. The source area of the transported mineral dust can be determined through specific chemical and physical analyses of aerosol, based on the typical soil composition of the different source regions [18,19].

The ground deposition phase of desert dust occurs as a result of local dynamics capable of activating a downward motion of the air mass. The onset of such dynamics coinciding with the arrival of a plume of desert dust can produce significant changes in the concentration of particulate matter in the boundary layer, with significant impacts on local physical and chemical conditions, thus decisively affecting air quality, with reduced visibility and effects on human health [20–23].

The use of satellite monitoring enables a comprehensive assessment of the contribution of desert dust to the atmosphere. One phenomenon that is clearly visible from satellites is the transport of Saharan dust across the nearby Atlantic Ocean into Central and South America by the intense easterly zonal circulations, that are typically present over west-central Africa. The desert dust transported contributes significantly to the biogeochemistry of the Atlantic and Amazonian area [11,24–26].

Additionally, the Mediterranean area and central and northern Europe are also frequently affected by desert intrusions [27]. The long-range transport of mineral dust can cause elevated concentrations of PM_{10} , which in some instances may contribute to exceedances of the limit values established by European legislation (Directive 2008/50/EC) [28–30]. In order to identify these contributions, which in some European countries—Spain, Italy, and Greece—can have a non-negligible impact [19,31–33], desert intrusion forecast services are available (Copernicus, <https://aerosol-alerts.atmosphere.copernicus.eu/>; AEMET, <https://dust.aemet.es/products/daily-dustproducts>, accessed on 20 October 2024).

Desert transport episodes in the Mediterranean Basin (MB) are more frequent during the spring and summer months. The seasonal variation of desert dust transport is determined by circulation climatology, which results in a recurrence of desert episodes between late winter and early spring in the eastern Mediterranean Basin (MB), in late spring in the central MB, and in late summer in the western MB [27]. With regard to Italy,

desert intrusions are more frequent in the south, with higher quantities than in central and northern Italy [33].

While most of the mineral dust intrusions in the MB and central and northern Europe originate from Saharan sources, a minority of these come from the Arabian Peninsula and, in rare instances, from western central Asia [27]. In March 2020, an anomalous transport of non-Saharan desert dust, attributable to the arid regions east of the Caspian Sea, occurred [34,35]. This intense episode affected Eastern Europe, the Balkan countries, and also Italy, where the desert dust caused the PM₁₀ limit value to be exceeded at numerous air quality monitoring stations, between 27 and 30 March 2020 [34].

In recent years, there has been an observable increase in the frequency and intensity of desert intrusions in the Mediterranean area [5,36]. A recent paper [37] highlights that during the winters of 2020–2022, several intense dust intrusions, originating from North Africa, impacted Europe with an unprecedented duration. The most significant impact of these events was observed in the western MB, with a notable increase in frequency compared to the period between 2003 and 2019. Furthermore, the paper examines the atmospheric circulation patterns during these episodes, postulating a shift in atmospheric circulation as a potential driver of the observed increase in Saharan dust intrusions over the western MB in February and March 2020–2022.

The current rapid climate change is associated with a change in the climatology of the main circulation patterns and their respective frequencies of occurrence [38], which in turn affects the mode and speed of climate change itself [39]. Such alterations in the prevailing atmospheric circulation patterns can give rise to variations in the frequency of mineral dust uplift and transport episodes, as well as in the distribution of source regions [5,36,37].

In this context, the present paper describes our recent studies, with the principal aim of deepening the analysis on central Italy, by considering the main desert dust intrusion events that occurred in the last six years (2018–2023). This work has been developed by performing statistical analyses for the estimation of the frequency of occurrence of such events, and by utilizing a weather-type classification in order to characterize all the events from the point of view of the respective underlining meteorological flux pattern.

This work is still in the first stage, nevertheless, relevant features emerged, regarding the seasonal variation of the desert dust events occurrence frequency and the recurrence of specific meteorological patterns in correlation with the onset of desert dust intrusions in the area under study.

In the present paper, the general structure of the implemented investigation framework is described together with a synthesis of the main results of the performed statistical analysis and of the weather-types-based dust events characterization. Moreover, in order to provide evidence of the significance of the recurring meteorological patterns in correspondence with desert dust intrusions, representative case studies are illustrated in detail, tracing the dust plume track evolution to the respective meteorological flux pattern.

2. Materials and Methods

2.1. Area and Period of Interest

In the present work, the Central MB area was studied, focusing in particular on the Tuscany region, Italy (Figure 1), in the six-year period from 2018–2023. In order to identify the main desert dust intrusions that occurred in this period over the area of interest, a hybrid approach was implemented by exploiting data both from a numerical forecast model, and from PM₁₀ observation stations. The model used was CHIMERE, provided by PREV’AIR (<http://www2.prevoir.org/>, accessed on 20 October 2024), while PM₁₀ observed data came from two background stations of the Tuscany Region Air Quality monitoring network managed by ARPAT (<https://www.arpat.toscana.it/temi-ambientali/aria/qualita-aria/>, accessed on 20 October 2024). The stations whose data were used in this study are IT1149A (PI-Montecerboli; lat 43.25, lon 10.88) and IT1681A (AR-Casa Stabbi; lat 43.66, lon 11.90), as shown in Figure 1.



Figure 1. Mediterranean Basin. Red border: area of interest, Tuscany region. Red dots, background stations, IT1149A (lat 43.25, lon 10.88) and IT1681A (lat 43.66, lon 11.90) of Tuscany Region Air Quality monitoring network.

The identification of the main dust episodes had the main goal of creating the dataset to be used in the subsequent analysis, and was performed in accordance with the methodologies employed by the European Community for estimating the dust contribution to PM_{10} (e.g., the European reference method for desert dust estimation, as from the Directive 2008/50/CE [28–30]) and with reference to the method proposed in [31,32] for the Italian territory (hereafter “Diapason-Methodology”). It must be pointed out that the present study is only concerned with the episode identification, rather than with the dust contributions quantification, which is instead targeted by the aforementioned methods.

2.2. Dust Days Dataset

The dust values estimated by the CHIMERE model allow for easy identification of episodes; however, the resolution of the adopted model is not sufficient for a detailed description of the deposition process. In some cases, where dust transport is confined to the higher levels of the atmosphere and conditions for ground deposition do not occur, an incorrect prediction of the deposition may cause false alarms. Hence, in order to avoid such false alarms, a check of the correct identification of desert contribution episodes was performed using the PM_{10} observed data from background stations. Only background stations located in rural areas were considered for this check, because desert episodes are better detectable in their data. The criterion adopted to determine the days affected by desert contributions was based on the selection of days on which the estimated dust values exceeded a threshold value, chosen as $5 \mu\text{g}/\text{m}^3$, with reference to the “Diapason-Methodology” [31,32]. The PM_{10} observed data were then used to confirm the consistency of the desert event (and hence to identify false alarms), by checking if the observed PM_{10} value on the selected days exceeded an empirical threshold value, chosen equal to the mean value over the period from 2018–2023, plus half a standard deviation. In accordance with the aforementioned criteria, days on which both conditions were met simultaneously were designated as dust days. In this way, we obtained a list of days affected by desert dust, diagnosed using model estimates and cross-checked using PM_{10} measurements for confirmation.

Days for which the model estimates exceeded the threshold of $5 \mu\text{g}/\text{m}^3$, but there was no match from the PM_{10} measurements, were considered false alarms (Properly false alarms were referred to the selection based on the model only). Conversely, days for which the model estimates remained below the threshold of $5 \mu\text{g}/\text{m}^3$, but the PM_{10} measured values exceeded the cross-check threshold (i.e., the mean value over the six-year period by a standard deviation), simultaneously at the two background stations, were considered missed alarms. These dust episodes can be verified by consulting other models, such as the MERRA2 reanalysis (https://fluid.nccs.nasa.gov/reanalysis/chem2d_merra2/, accessed on 20 October 2024), NOAA Hysplit model (<https://www.ready.noaa.gov/HYSPLIT.php/>, accessed on 20 October 2024), ensemble of the CAMS (https://atmosphere.copernicus.eu/charts/packages/cams_air_quality/, accessed on 20 October 2024), MONARCH model

(<https://dust.aemet.es/about-us/monarch#daily-dust-service/>, accessed on 20 October 2024), and SKYRON model (<https://forecast.uoa.gr/en/forecast-maps/dust/>, accessed on 20 October 2024).

The comprehensive examination of the whole dataset with dust days, and false and missed alarms allowed for an assessment of the employed selection methodology.

2.3. Weather Types Classification

The availability at Consorzio LaMMA of a recently implemented weather types classification—PCT—was exploited to relate the selected dust episodes with the corresponding meteorological patterns, at both the synoptic and the local level [40].

PCT09 is a nine classes classification built by utilizing the mean sea-level pressure field (MSLP) as the main predictor and using the COST733class-1.2 classification software package [41]. The nine classes of PCT09 classification are described in Table 1, and the corresponding MSLP patterns are shown in Figure 2 through representative centroids.

Table 1. Description of the main features of the nine classes (centroids) of PCT09 classification.

Circulation Types	Description
CT1	High pressure over central–northern Italy, weak low over Ionian Sea with easterly flow
CT2	Orographic low pressure over Adriatic Sea with strong north-easterly flow
CT3	High pressure with maximum values over northern–eastern Italy with no pressure flow
CT4	Orographic low pressure over Ligurian or northern Tyrrhenian Sea with strong southerly flow
CT5	High pressure with maximum values over north–western Italy, weak low over Ionian Sea with no pressure flow
CT6	High pressure over central–southern Italy, low pressure over Alpes with westerly zonal flow
CT7	Orographic low pressure over northern Italy, with strong westerly or north–westerly flow
CT8	High pressure with light southerly flow
CT9	High pressure over northern Italy, weak low over central–southern Italy with easterly flow

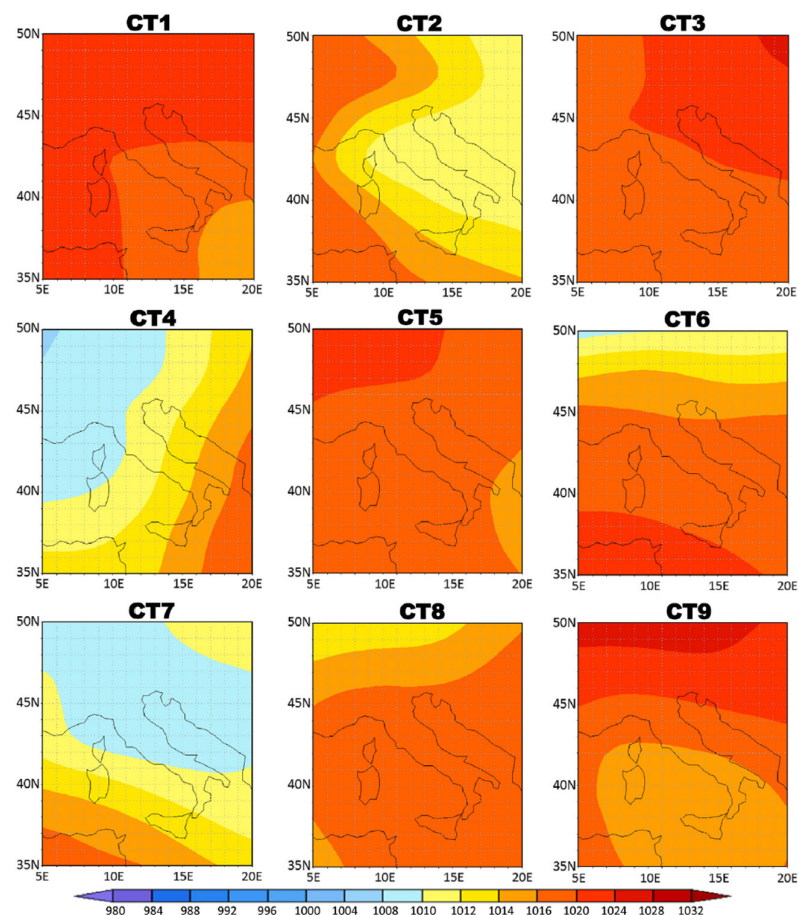


Figure 2. Maps of the representative (centroids) MSLP patterns of the nine classes of PCT09 classification.

3. Results

The results of the statistical analysis of the desert dust episodes obtained by applying the selection methodology described in the previous section are presented below. In particular, the seasonal distribution of the detected episodes and missed and false alarms, in different years and over the whole period, is analyzed. Furthermore, the episodes are correlated with the weather types classification, PCT09, in order to highlight the most recurrent meteorological configurations at desert intrusions. Finally, some case studies for relevant desert dust episodes are described to illustrate their correlation with the corresponding atmospheric circulation patterns.

3.1. Dataset Analysis

The total number of dust days identified over the six-year period from 2018–2023 was 263 days, corresponding to an average of 44 days per year. A total of 74 episodes can be identified, consisting of a variable number of consecutive dust days, between 2 and 6 days. The number of episodes per year is also variable, ranging from 10 to 15. These results, summarized in Table 2, are in line with those reported in the literature for the Tuscany region [33].

Table 2. Dust intrusions during the analyzed period 2018–2023.

Analyzed Period	6 Years 2018–2023
Dust intrusions	74 episodes, 263 days
Dust days per year	44 days
Dust intrusions per year	10–15 episodes, 2–6 days

In most cases, false alarms take place immediately before or immediately after dust days (about 70 per cent of cases). In a smaller number of instances, however, there are false alarms not close in time to dust days. In both cases, desert dust is present (due to long-range transport) at high altitude but does not settle on the ground.

Missed alarms can occur far in time from dust days. In such cases, missed alarms could be traced to an inaccurate model simulation of the dust lift and subsequent transport processes. However, in cases where the missed alarms occur immediately after a dust day, the observed high PM₁₀ concentrations values can be attributed to the resuspension of desert dust particles transported on site on the previous days and trapped in the boundary layer. This resuspension also occurs after the end of the transport phenomenon. Hence, in these cases, the occurrence of the missed alarm could be traced to the incorrect simulation of boundary layer dynamics by the model.

Table 3 and Figure 3 show the number of dust days, of missed alarms and of false alarms identified by applying the adopted method as outlined above, for each year and for the entire period. For the corresponding dust days, the missed and false alarms percentage values were obtained as the ratio to the respective total number of dust and missed and false alarm days in each year.

Table 3. Dust days, missed alarms, and false alarms for each year and for the whole period from 2018–2023. Percent is normalized, respectively, to the total number of dust and missed and false alarms days for each year.

Years	Dust Days		Missed Alarms		False Alarms		Total Days	
2018	68	59%	8	7%	39	34%	115	100%
2019	41	60%	9	13%	18	26%	68	100%
2020	31	53%	11	19%	16	28%	58	100%
2021	40	75%	1	2%	12	23%	53	100%
2022	45	64%	6	9%	19	27%	70	100%
2023	38	73%	6	12%	8	15%	52	100%
2018–2023	263	63%	41	10%	112	27%	416	100%

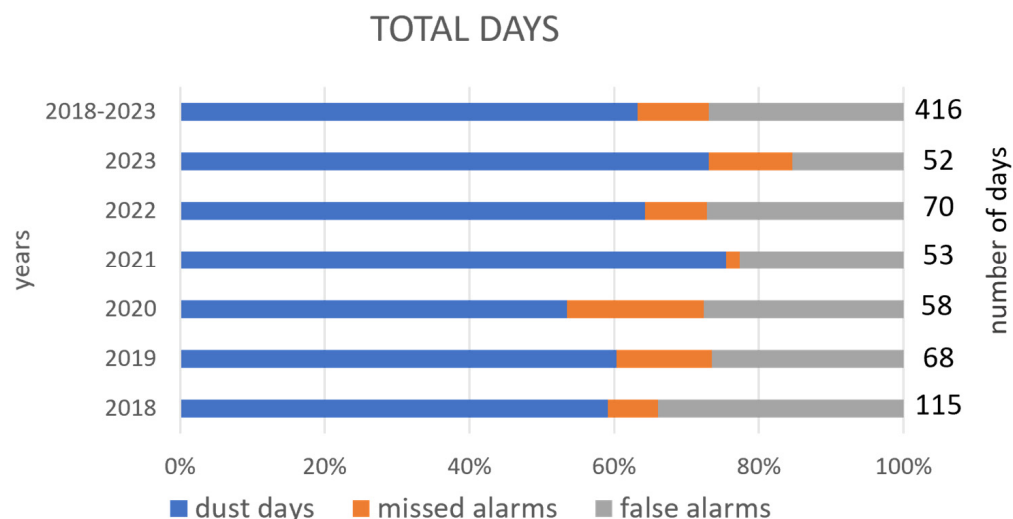


Figure 3. Percentage of dust days (blue), missed alarms (orange), and false alarms (grey), for the whole period from 2018–2023 for each year. Percentage values are normalized to the corresponding total number of days for the whole period and for each year, reported on the right of each respective diagram.

Missed alarms average 10% of total days, and false alarms about 30%, with inter-annual variability.

The number of dust days and false alarms in 2018 is higher than in subsequent years; furthermore, in 2023, there is a significant reduction in the false alarm rate (Table 3, Figure 3). These results could be due to an upgrade of the CHIMERE model improving its dust prediction performance since 2018, and especially in 2023.

The following Figures (Figures 4–6) show histograms of the number of dust days, and false and missed alarms on a seasonal basis (winter, jan–mar; spring, apr–jun; summer, jul–sept; autumn, oct–dec), for each year and for the entire six-year period. The histograms in Figure 4 show the seasonal percentage of dust days, normalized to the total number of dust days occurring in each year, reported on the right of each respective diagram. Dust days occur more frequently in spring and summer, in accordance with the literature for the Central Mediterranean area [27]. Similarly, Figures 5 and 6 show the percentage, evaluated on a seasonal basis, of false alarms and missed alarms, respectively. In the period from 2018–2023, there are 112 false alarms, with a prevalence in spring and summer. Compared with dust days (Figure 4), there is an increase in the frequency of occurrence of false alarms during the autumn (Figure 5). With regard to missed alarms, with 41 days in total for the whole six-year period, Figure 6 shows significant variability from year to year, with a prevalence of missed alarms in the cold season, and a very low frequency of occurrence in spring.

Thanks to the use of observed data from background stations, the adopted dust days identification method is not affected by the problem of false alarms, which would be relevant if the identification was based only on model estimates. However, to further reduce missed alarms, the method could be improved by adopting more than one model, i.e., not only the CHIMERE model, but also, e.g., the ensemble of CAMS, MONARCH, or SKYRON models.

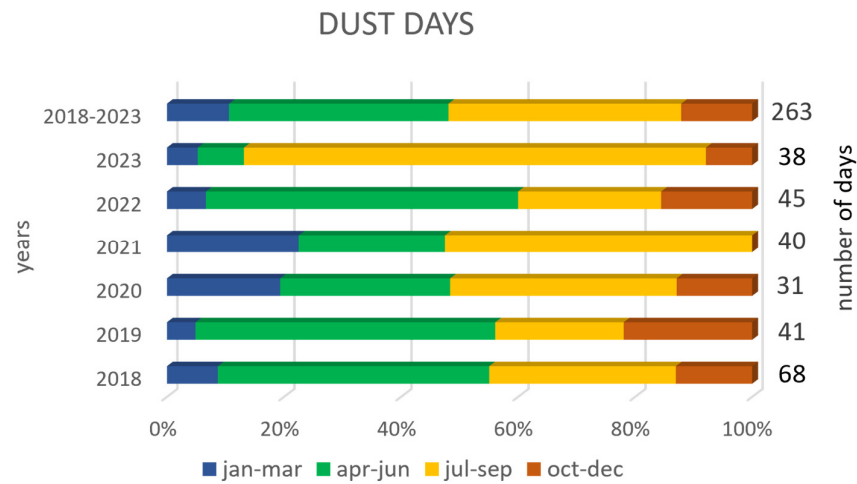


Figure 4. Seasonal frequency of dust days: for the whole period from 2018–2023 for each year. Percentage values are normalized to the respective total number of dust days in the whole period and for each year, reported on the right of each respective diagram.

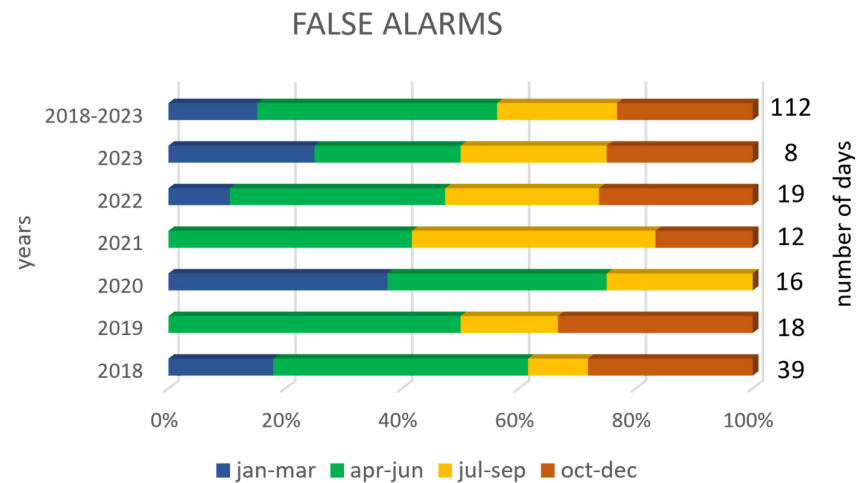


Figure 5. Seasonal frequency of false alarms: for the whole period from 2018–2023 for each year, the number of false alarms is reported. Percentage values are normalized to the respective total number of dust days in the whole period and for each year, reported on the right of each respective diagram.

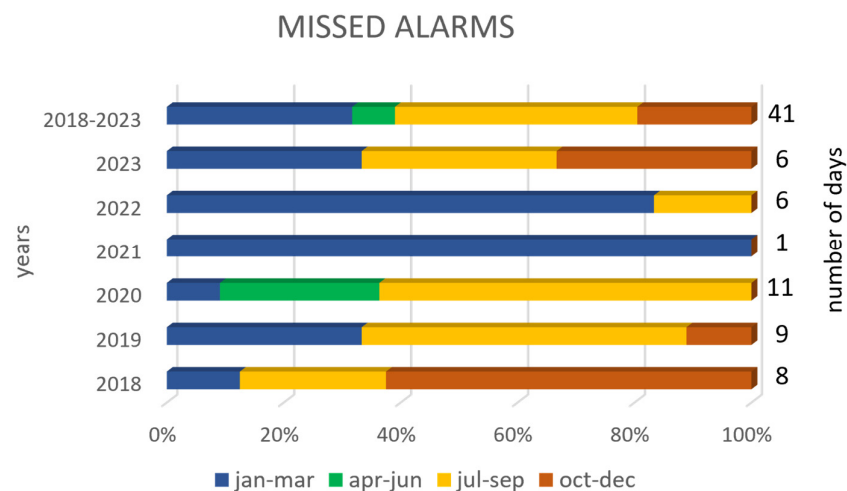


Figure 6. Seasonal frequency of missed alarms: for the whole period from 2018–2023 for each year, the number of missed alarms is reported. Percentage values are normalized to the respective total number of dust days in the whole period and for each year, reported on the right of each respective diagram.

3.2. Relation with Weather Types PCT09

The frequency of the weather types from the PCT09 classification (Figure 2, Table 1) was computed for dust days, and false and missed alarms over the six-year period from 2018–2023, and the results are shown in Figure 7. The percentage values were normalized to the total number of days for each group, respectively, the whole period (2191 days), the dust days (263 days), the false alarms (112 days), and the missed alarms (41 days).

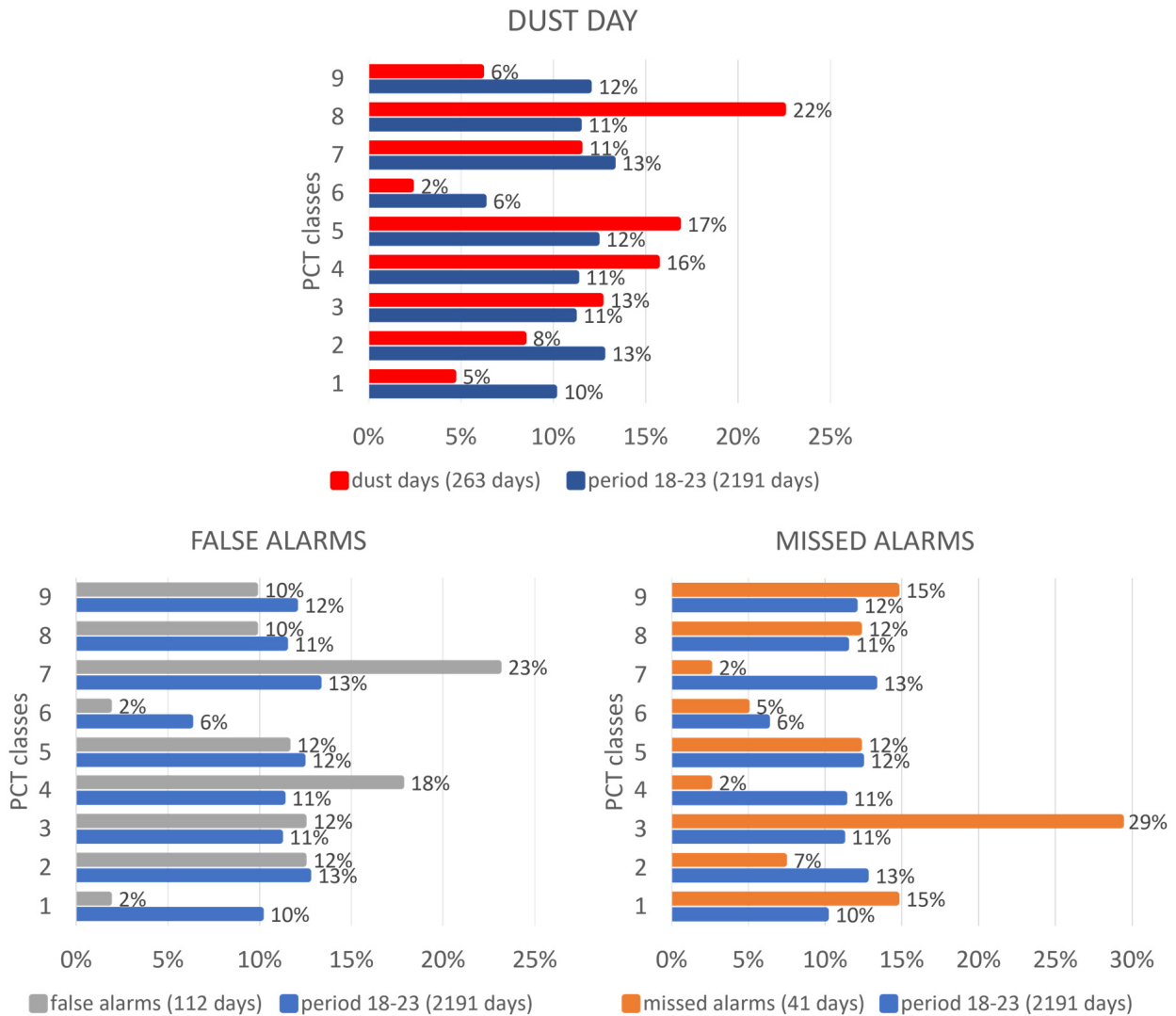


Figure 7. Frequency of PCT classes in the six-year period from 2018–2023 (blue) in the dust days (red), in the false alarms (grey), and in the missed alarms (orange), over the entire period. The percentage is normalized to the total number of days of each group, respectively.

Considering the whole dataset for the six years, almost all classes of weather types, with the exception of CT6 (high pressure over central–southern Italy, low pressure over Alpes with westerly zonal flow) and CT1 (high pressure over central–northern Italy, weak low over Ionian Sea with easterly flow), show a similar frequency of occurrence, with values ranging between 10% and 13%. Considering the dust days group, the most prevalent class is CT8 (high pressure with light southerly flow). With regard to false alarms, the most frequent classes are CT7 (orographic low pressure over northern Italy, with strong westerly or north-westerly flow) and CT4 (orographic low pressure over Ligurian or northern Tyrrhenian Sea with strong southerly flow), while for missed alarms, the CT3 (high pressure with maximum values over northern–eastern Italy with no pressure flow) class is the most frequent (Figure 7).

The greater recurring classes during dust days and missed alarms, CT8 and CT3, respectively, are related to anticyclonic circulations, that typically favor dust deposition. Regarding the false alarms, there is a high incidence of CT7 and CT4. From the point of view of the respective atmospheric circulation pattern, CT7 corresponds to a flux from west–northwest, favoring the entrance of Atlantic air masses, while CT4 corresponds to a southerly flux, favoring dust transport from North Africa. Differently from markedly anticyclonic configurations, both of these flux patterns are more compliant with dust transport without deposition. Each episode of dust intrusion is made up of more than one day. These correspond to the phase when relevant amounts of particulate matter are extracted from the high-altitude plume and reach the lowest levels of the atmospheric boundary layer, where they settle on the surface in a specific target area. This phase, on a given target area, is sometimes preceded and/or followed by a phase of high-altitude transport without dust deposition that, in our approach, are identified as false alarm days immediately adjacent in time to dust days. Hence, it is plausible that in our analysis focused on the Central Mediterranean area, such false alarms are mainly correlated with southerly or westerly fluxes. A southerly flux (as in CT4) can be responsible for desert dust transport coming from the Saharan source area and heading directly to the Central Mediterranean area. This represents the “direct” and more frequent configuration for Saharan dust intrusion over Italy. A westerly flux (as in CT7) can be responsible for “indirect” transport over the Mediterranean Sea of a Saharan dust plume, previously injected over the Atlantic Ocean by the strong easterly atmospheric fluxes frequently occurring from the Sahara through to the west African coasts.

Additionally, the frequency of the PCT classes was calculated on a seasonal basis, and the percentage was normalized to the total number of days, for each season. For example, during the summer, the frequency of the PCT classes for the total days was normalized to 552 days; for dust days, to 105 days; for false alarms, to 24 days; and for missed alarms, to 17 days (Table 4).

Table 4. Number of days and prevalent PCT class for the total days in 2018–2023, the dust days, the missed alarms, and false alarms, in each season and in the whole period.

	Period 2018–2023		Winter		Spring		Summer		Autumn	
	PCT	Days	PCT	Days	PCT	Days	PCT	Days	PCT	Days
Total days	2, 3, 4, 5, 7, 8, 9	2191	1, 9	541	7, 8, 5	546	2, 5	552	3, 4	552
Dust days	8	263	3	27	8, 4, 5	99	8	105	3, 8	32
False alarms	7, 4	112	7, 4, 3	17	7, 4	46	2	24	3, 9	25
Missed alarms	3	41	3	13	3	3	1, 3, 9	17	3, 8, 2	8

The frequency of the PCT classes during the six-year period shows a typical seasonal variation: during the winter, the most frequent classes are CT1 (high pressure over central–northern Italy, weak low over Ionian Sea with easterly flow) and CT9 (high pressure over northern Italy, weak low over central–southern Italy with easterly flow); in spring, the CT7 (orographic low pressure over northern Italy, with strong westerly or north–westerly flow), CT8 (high pressure with light southerly flow) and CT5 (high pressure with maximum values over north–western Italy, weak low over Ionian Sea with no pressure flow); in summer, the CT2 (orographic low pressure over Adriatic Sea with strong north–easterly flow) and CT5 (high pressure with maximum values over north–western Italy, weak low over Ionian Sea with no pressure flow); and in autumn, the CT3 (high pressure with maximum values over northern–eastern Italy with no pressure flow) and CT4 (orographic low pressure over Ligurian or northern Tyrrhenian Sea with strong southerly flow) (Figure 8).

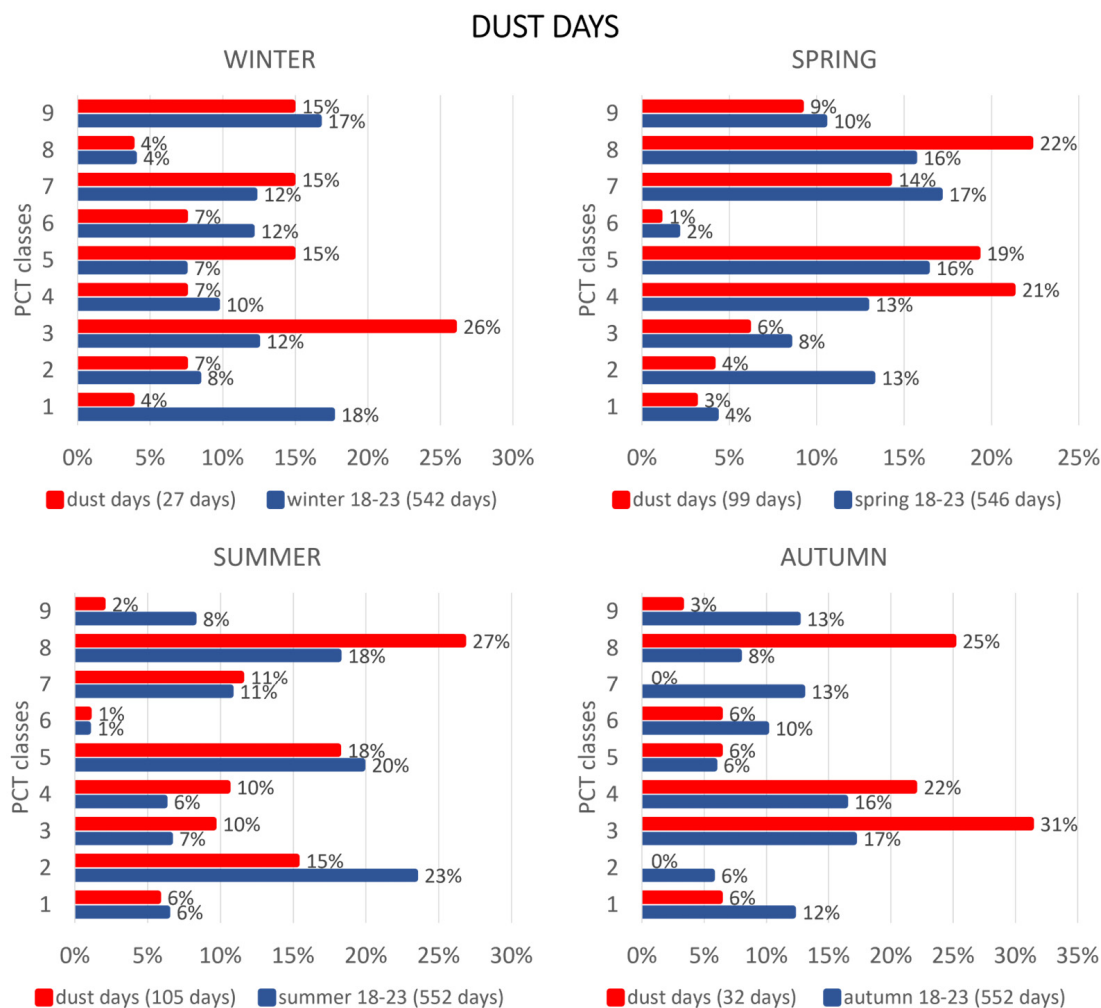


Figure 8. Frequency of PCT classes in the six-year period from 2018–2023 (blue) and in the dust days (red), on a seasonal basis. The percentage is normalized to the total number of days of each group, respectively.

During dust days, CT3 and CT5 are more frequent in winter, CT8, CT4, and CT5 in spring, CT5 and CT8 in summer, and CT3 and CT8 in autumn (Figure 8). In all seasons, the anticyclonic classes conducive to deposition are more prevalent, with the exception of CT4, which, as previously stated, is compatible with a southerly flow and, therefore, with Saharan transport.

Regarding false alarms, the most frequent classes are CT7, CT4, and CT3 in winter, CT7 and CT4 in spring, CT2 in summer, and CT3 and CT9 in autumn. In the winter and autumn, only class CT3 is anticyclonic; the others (CT7, CT4, CT2, and CT9) are characterized by orographic flows from the west or northeast, which may be related to transport without deposition. The most frequent class for missed alarms is CT3 in all seasons, with CT8 and CT2 also recurring in autumn. The first two classes are anticyclonic and favor deposition, while CT2 corresponds to a north-easterly flow.

The figures of the seasonality frequency of PCT classes for false and missed alarms are reported in the Supplementary Materials (Figures S1 and S2), as well as the complete table of the seasonality frequency of PCT classes (Table S1).

Even on a seasonal basis, there are notable differences between the frequency of occurrence of PCT09 classes on dust days, and false and missed alarms. Class CT8 is a reliable indicator of dust days during the spring and summer seasons. However, Class CT3 presents a challenge in terms of attributing its occurrence, in particular during the colder

semester, where it is frequently associated with both dust days and false and missed alarms. Conversely, during the warmer semester, it is predominantly linked to missed alarms.

Given that dust episodes typically persist for several days, it is not feasible to trace each episode to a single PCT class. Each such episode corresponds to a sequence of PCT classes, typically anticyclonic and conducive to deposition during dust days, compatible with transport without deposition in preceding phases. It should be noted that the predominant direction of the origin of the dust is south–southwest (“direct” case), but west–northwest flows are also frequent (“non-direct” case).

3.3. Case Studies

The notable prevalence of “non-direct” desert episodes prompts an investigation into particularly interesting cases related to the omega configuration. Indeed, the latter represents a blocking condition, occurring with a higher frequency in February and March. As a consequence of climate change, the frequency and duration are both increasing [42].

Here below, three cases studies from the set of dust episodes identified in the five six-year 2018–2023 dataset are described as examples illustrating part of the dynamical variability of the events. The first case study exemplifies a “direct” Saharan dust event, representing one of the most prevalent configurations. The other two are “non-direct” Saharan dust events, characterized by the omega structure. The case studies are schematically illustrated by GFS reanalysis maps, MERRA-2 reanalysis, and NOAA Hysplit backward trajectories.

3.3.1. Case Study 1—Direct Saharan Dust Event—May 2020

As the first case, a direct Saharan dust event is considered that took place from 13 to 15 May 2020. During these days, a south-westerly flow drove the Saharan dust over the Central Mediterranean area, crossing the Tyrrhenian Sea and impinging on the western side regions of Italy. From the observed data in correspondence with the two selected sampling stations, during the period of this case study, the main PM concentration peak occurred on May 14th (CT4), with a local wind average direction observed from south–west (Figure 9).

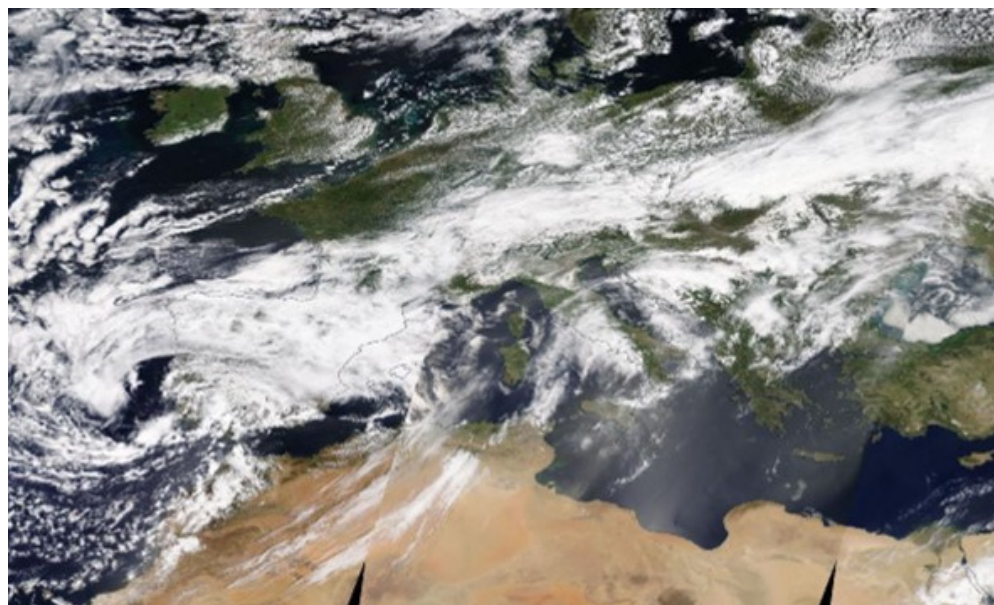


Figure 9. Satellite images composite from Terra MODIS Corrected Reflectance (true-color) imagery for 14 May 2020 (ref) [<https://worldview.earthdata.nasa.gov>, accessed on 20 October 2024].

The synoptic situation leading to this dust event is reported in Figure 10, showing the baric configurations for a few antecedent days. It is characterized by the evolution of a structured low-pressure system over the eastern Atlantic, extending through the western Iberian Peninsula, and by the further presence of a high-pressure area over the central-

eastern Mediterranean Sea. In accordance with this pressure field pattern, a strong westerly flow can be diagnosed over the central Mediterranean Sea, as from the 500 hPa geopotential field (color shading) shown in Figure 10. This flow condition is particularly evident in the bottom left and right panels, valid for 12 UTC of 13th and 14th May, respectively. The lifting of Saharan desert dust in this event can be traced to the development of a secondary local low-pressure system, between Morocco and Algeria, related to the main low-pressure system and to intervening mid-tropospheric cold air infiltrations. Such a secondary low can be recognized in the surface pressure pattern (white isolines) in the top-right and bottom-left panels of Figure 10, valid for 12 UTC of 12th and 13th May, respectively.

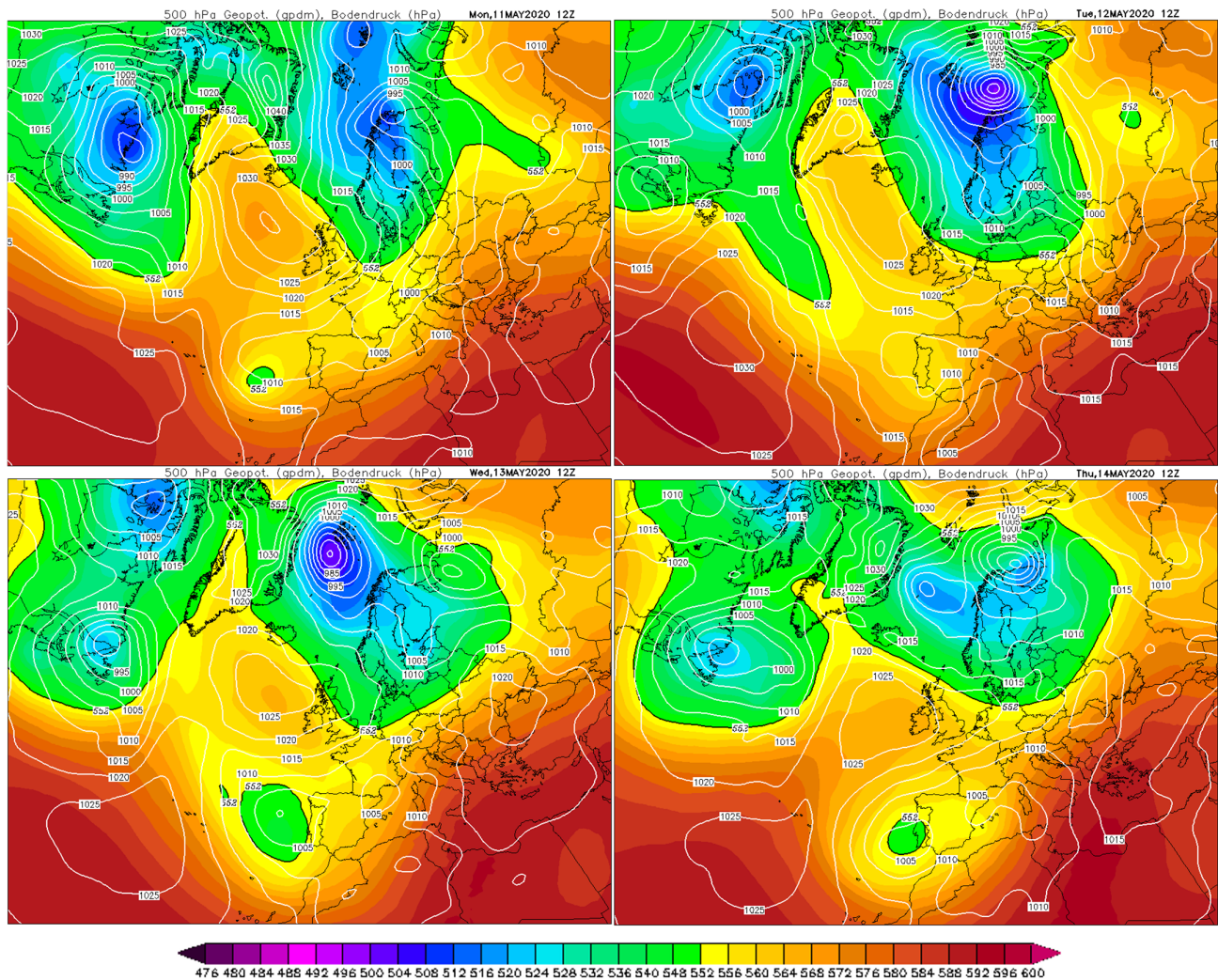


Figure 10. GFS reanalysis maps of 500 hPa geopotential (color shading) and surface pressure (white isolines) fields, for 11, 12, 13, and 14 May 2020 at 12 UTC (maps from: <https://www.wetterzentrale.de/en/reanalysis.php?model=cfsr>, accessed on 27 November 2024).

The transport of the lifted Saharan desert dust by the strong south-westerly winds from Algeria to the Central Mediterranean area can be seen in the left panel of Figure 11, showing the dust mass content on the whole air column, estimated from the MERRA 2 dataset for 00 UTC of 14 May. The corresponding dust concentration at the surface level, peaking in central Italy, can be seen in the right panel of Figure 11, estimated from the MERRA 2 dataset for the same hour. The type of weather assigned to this day is PCT4, which is generally associated with moderate–strong winds from the southwest. Looking at Figure 10 (bottom right), however, we note that in this case, there was a weak baric gradient with light winds favorable to the deposition of dust.

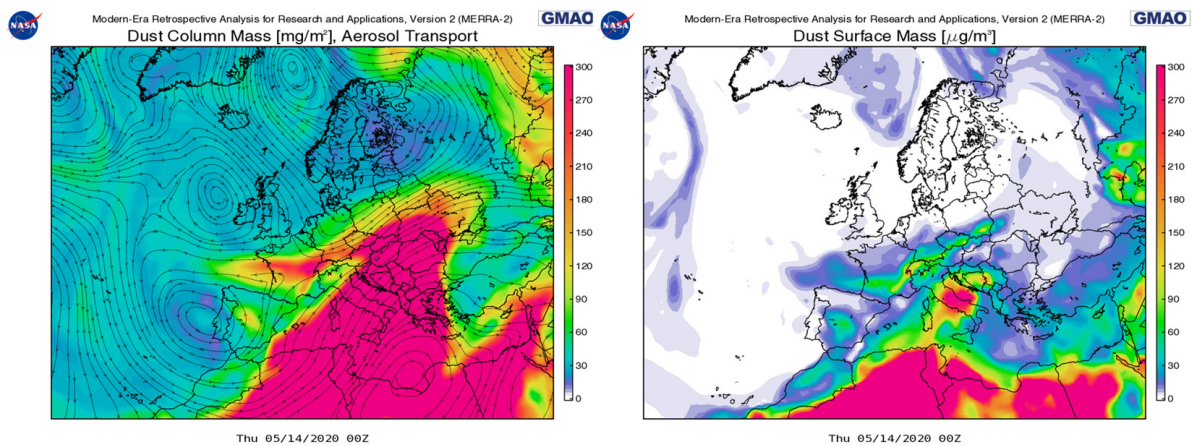


Figure 11. MERRA 2 dust column mass (left) and dust surface mass (right) maps for 14 May 2020 at 00 UTC.

This dust transport dynamics reconstruction is confirmed by the back-trajectories from the NOAA HYSPLIT model shown in Figure 12. These were generated by setting the terminal location in correspondence with our study area in the Tuscany region at 15 UTC of 14 May.

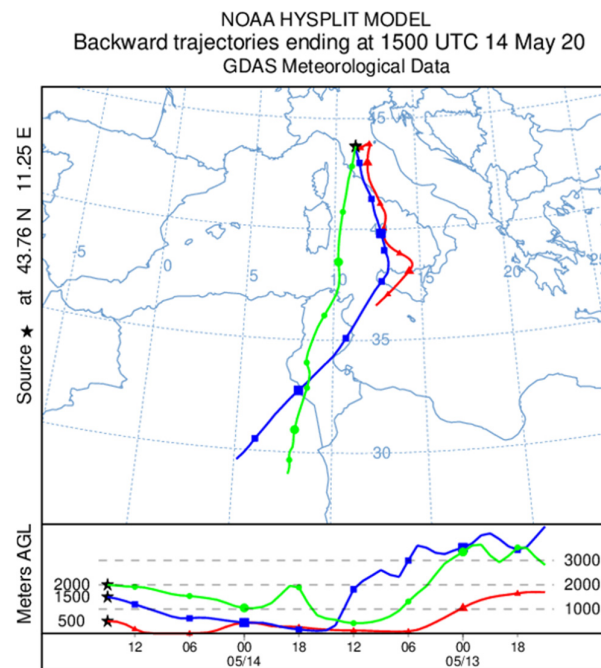


Figure 12. NOAA HYSPLIT back-trajectories estimated for 14 May 2020 at 15 UTC. The lines represent the trajectories of a particle starting at different altitudes (500, 1500, and 2000 m for the red, blue, and green lines, respectively). The bottom panel shows the altitude of the particles over time.

3.3.2. Case Study 2—Non-Direct Saharan Dust Event—February 2019

This case is characterized by a strong high-pressure ridge centered on Italy, surrounded at lower latitudes by two low-pressure centers conferring a characteristic omega-like shape to its pressure pattern, as visible in the left panel of Figure 13, valid for 17 February 2019 at 12 UTC. In the right panel of Figure 13, a satellite composite from Terra MODIS Corrected Reflectance (true-color) imagery is shown for 18 February 2019. A clear-sky area is present with borders all along a wide arc running from western Europe, passing through central-northern European states, and reaching the Black Sea on the eastern side. The presence of particulate matter can be identified on many portions of such an arc, especially over

northern Europe, Italy, and the northern Adriatic Sea. Accordingly, measurements from the observing stations of the Tuscany region utilized in this study give peak PM concentration values on 18 February, continuing with gradually lower values on 19 February.

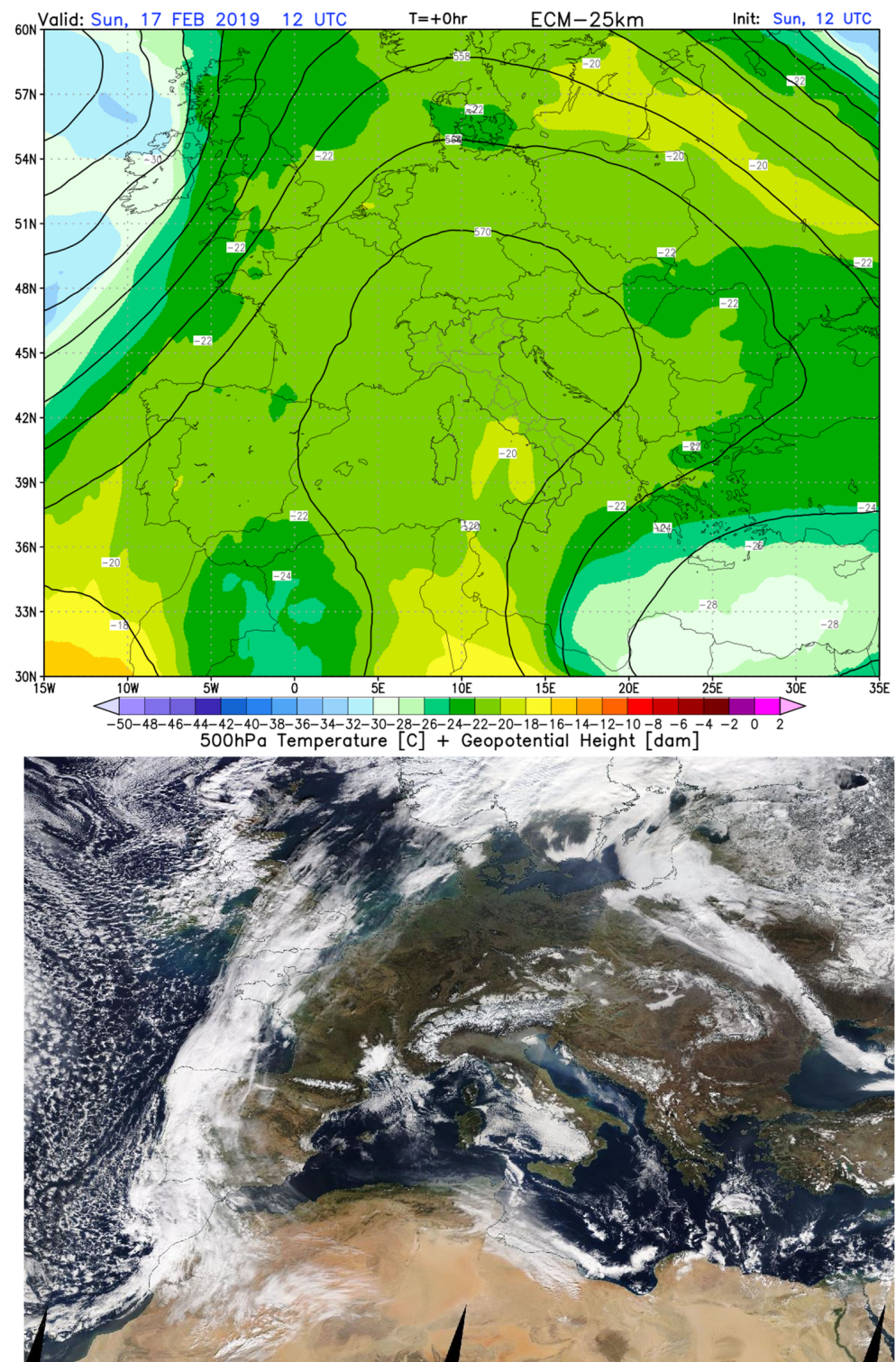


Figure 13. Upper panel: 500 hPa geopotential and temperature fields from the 25 Km resolution ECMWF global model are shown for 12 UTC of 17 February 2019. Bottom panel: satellite images composite from Terra MODIS Corrected Reflectance (true-color) imagery for 18 February 2019 (<https://worldview.earthdata.nasa.gov>, accessed on 20 October 2024).

The evolution of the meteorological conditions of this case is shown in Figure 14, with four panels for 12 UTC of 15, 16, 17, and 18 February 2019. The high-pressure ridge over the central Mediterranean Area persists in the area for several days, as also confirmed by anticyclonic PCT classes (15, 16, 17, and 18 February 2019, CT3, CT1, CT5, CT8, respectively). The low-pressure center on the left side of the omega-like pressure pattern contributes to generating the flux of Saharan desert dust and to driving it towards the eastern Atlantic. There sustained winds, corresponding to the relevant pressure gradient all along the arc around the high-pressure center, drive such Saharan dust along a curved track across Europe reaching the eastern region over the Black Sea, where part of it is then transported to Italy by the action of north-westerly winds produced by the low-pressure center on the right side of the omega-like pressure pattern.

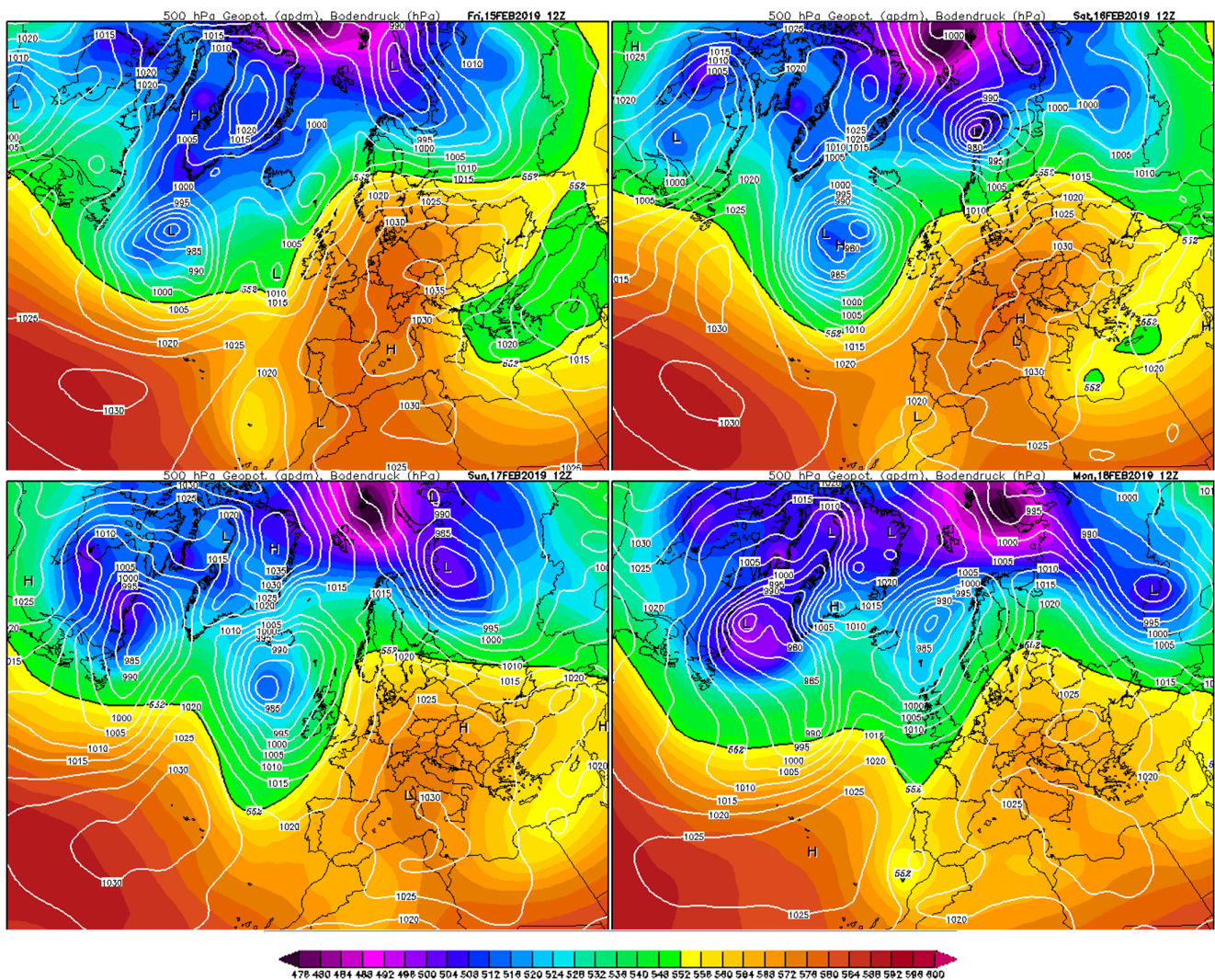


Figure 14. GFS reanalysis maps of 500 hPa geopotential (color shading) and surface pressure (white isolines) fields, for 15, 16, 17, and 18 February 2019 at 12 UTC. (maps from: <https://www.wetterzentrale.de/en/reanalysis.php?model=cfsr>, accessed on 27 November 2024).

The long journey of the Saharan dust matter, circling up to the high latitudes of the Scandinavian peninsula, then down to the lower latitudes of the Black Sea and finally to Italy from the east, is well illustrated by the plots of Figure 15, showing the total column dust matter and the corresponding surface deposition, from the MERRA archive for 18 February 2019, the day of the maximal measured PM concentration in Tuscany.

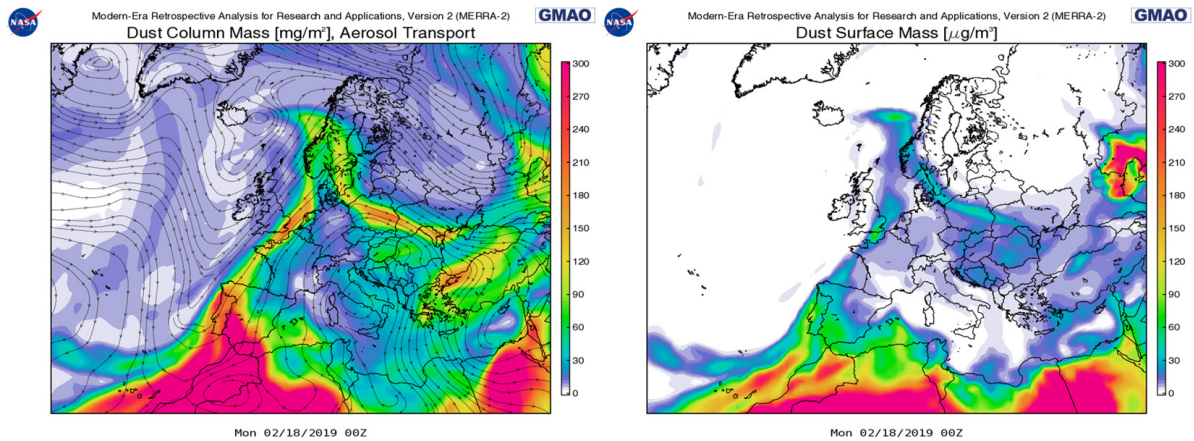


Figure 15. MERRA 2 dust column mass (left) and dust surface mass (right) maps for 18 February 2019.

The computed NOAA HYSPLIT back-trajectories of Figure 16 give further confirmation of these dynamics, showing the last portion of the long track of an atmospheric tracer arriving in Tuscany at about 14 UTC on 18 February 2019 (CT8). The shown back-trajectories provide evidence that, after having been brought to the east of Europe, the dust is carried back towards Italy by easterly winds, evidencing the non-direct type of this Saharan dust episode. Moreover, a further detail emerges regarding the very last part of the track: due to a very local circulation pattern, linked to the presence of the high-pressure center and its interaction with the local orography, the dust matter is brought to Tuscany by south-westerly winds, after a clockwise turn of the flux in the very proximity of central Italy, south of Tuscany.

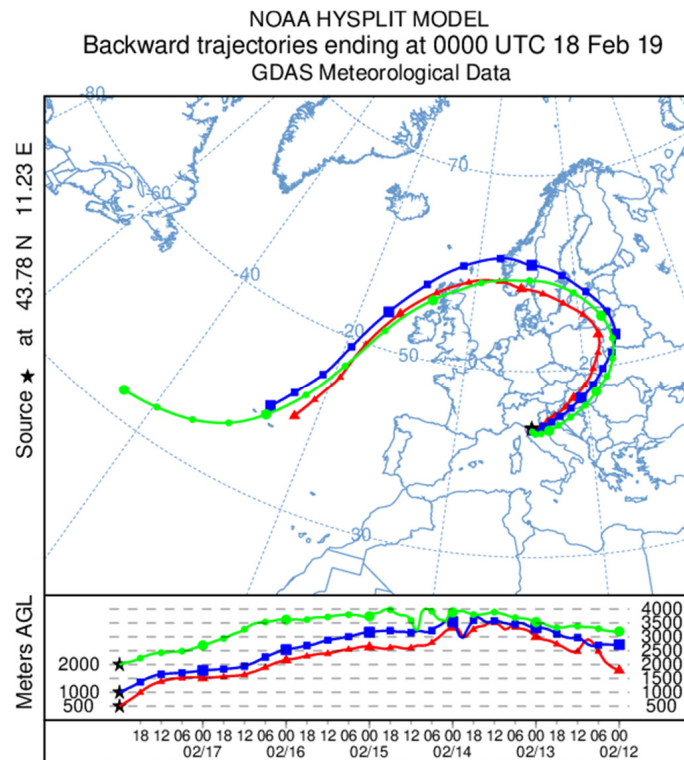


Figure 16. NOAA HYSPLIT back-trajectories estimated for 18 February 2019, at 00 UTC. The lines represent the trajectories of a particle starting at different altitudes (500, 1000, 2000 m for the red, blue, and green lines, respectively). The bottom panel shows the altitude of the particles over time.

3.3.3. Case Study 3—Non-Direct Saharan Dust Event—February 2021

This case consists of a non-direct Saharan dust episode, because it can be characterized by a northerly provenience on the Italian peninsula of the Saharan particulate matter, with deposition on the Tuscany Region beginning on 23 February 2021, reaching peak PM concentration values on 24 February and continuing with a gradual decrease to 27 February. It must be pointed out that, during the month of February 2021, several strong wind events took place in the Saharan region that lifted into the atmosphere huge amounts of dust [37], subsequently spread by the winds to wide portions of the Atlantic Ocean and western Europe. Record peak values of measured PM concentration were recorded not only in the nearby Canary Islands, but also in the Iberian Peninsula and in France [37]. The event considered here corresponds to the terminal part of the sequence that took place in February 2021 and is the one with the highest impact on the Tuscany region.

The meteorological conditions during the days of maximal dust deposition are shown in Figure 17. In the left panel the 500 hPa geopotential and temperature fields from the 25 Km resolution ECMWF global model are shown for 00 UTC of 23 February 2023, evidencing a typical omega-like pressure pattern, with a deeply northward-extending pressure ridge centered on Italy and Balkan area, surrounded by two low-pressure systems in its westward and eastward flanks. This kind of configuration produces a sustained and persistent northward flux on its westward flank, frequently inducing a relevant transport of Saharan dust on western and central Europe and, especially, on Italy. In the right panel of Figure 17, a satellite images composite from Terra MODIS Corrected Reflectance (true-color) imagery is shown for the subsequent day (24 February). The presence of the dust is evident over most of western and central Europe and the Mediterranean basin, in rough coincidence with the high-pressure ridge, that appears in turn surrounded by thick frontal clouds systems.

The dynamics conducting to such a configuration are shown in Figure 18. On the westward side of the high-pressure ridge, a deep trough, driven by a relevant low-pressure system in the northern Atlantic, penetrates down across the Iberian Peninsula to Morocco (top-left panel of Figure 18, valid for 21 February at 12 UTC), determining a cut-off low (top-right panel of Figure 18, valid for 22 at 06 UTC) then moving South in central Algeria, that constitutes the westward flank of the omega-like pattern and contributing to a further lifting of Saharan dust during its southward evolution (bottom panels of Figure 18, valid for 23 and 24 February both at 12 UTC)

The circulation induced by the trough over the Atlantic, West of Iberian Peninsula, in combination with the high-pressure ridge over Mediterranean Sea centered right over central-northern Italy, drives a large amount of desert dust along a track covering Spain, then France, and then Italy, as evidenced in the left panel of Figure 19. In this condition, a relevant dust deposition can be seen all along the track, bringing the Saharan desert dust onto most of the Italian peninsula with a local northeasterly provenience. Such a track is evidenced by the surface dust pattern shown in the right panel of Figure 19, and confirmed by the back-trajectories reported in Figure 20. In particular, Figure 20 shows that all three trajectories reach the target area with a north-eastern origin, even if the green and red lines show that part of northern Italy is affected by a direct injection of dust. On the other hand, PCT3 on the days before February 24 and on the day of maximum dust deposition confirm a high-pressure circulation favorable for dust deposition with a weak eastern circulation.

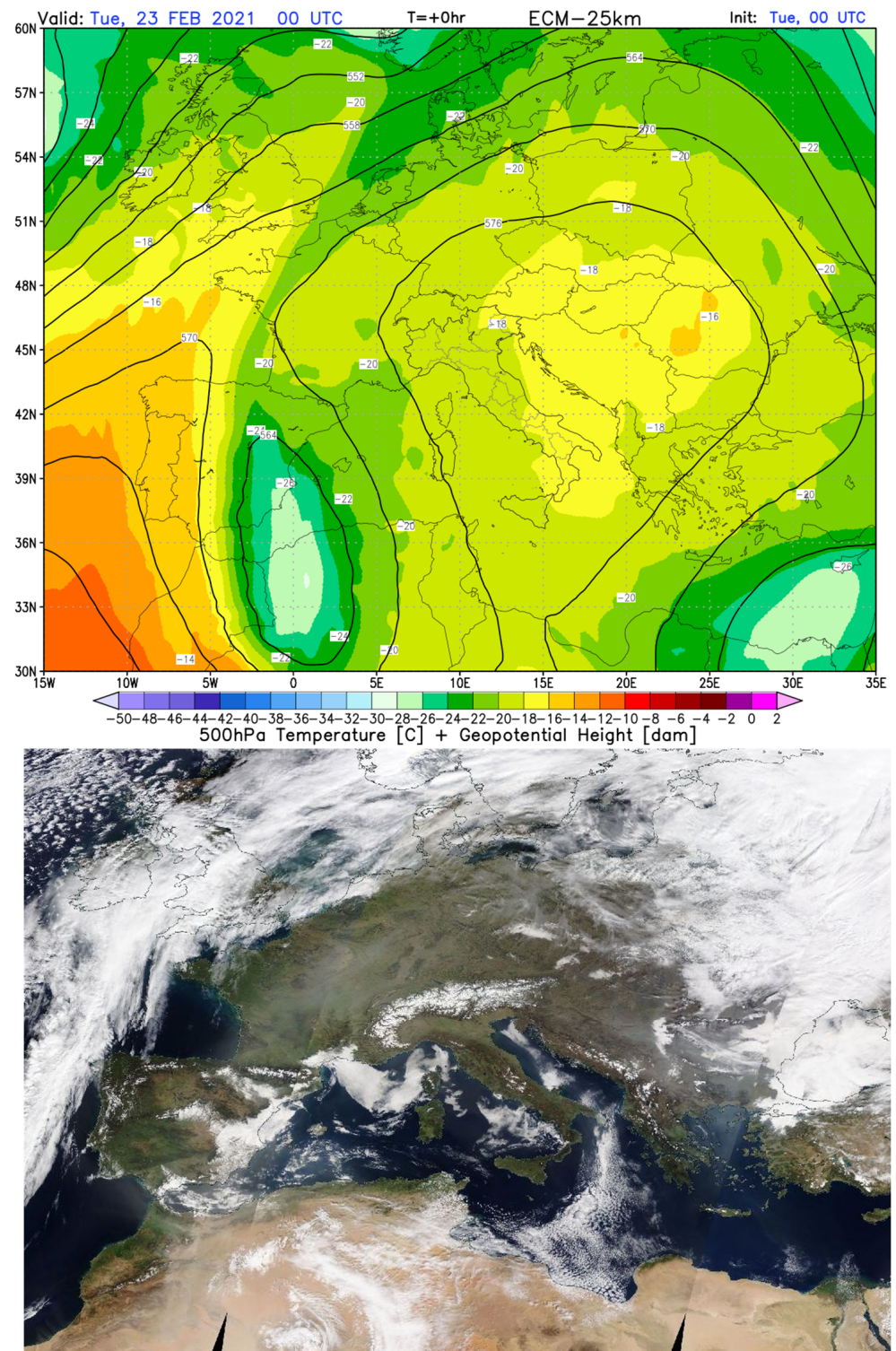


Figure 17. Upper panel: 500 hPa geopotential and temperature fields from the 25 Km resolution ECMWF global model are shown for 00 UTC of 23 February 2021. **Bottom panel:** satellite images composite from Terra MODIS Corrected Reflectance (true-color) imagery for 24 February 2021 (<https://worldview.earthdata.nasa.gov>, accessed on 20 October 2024).

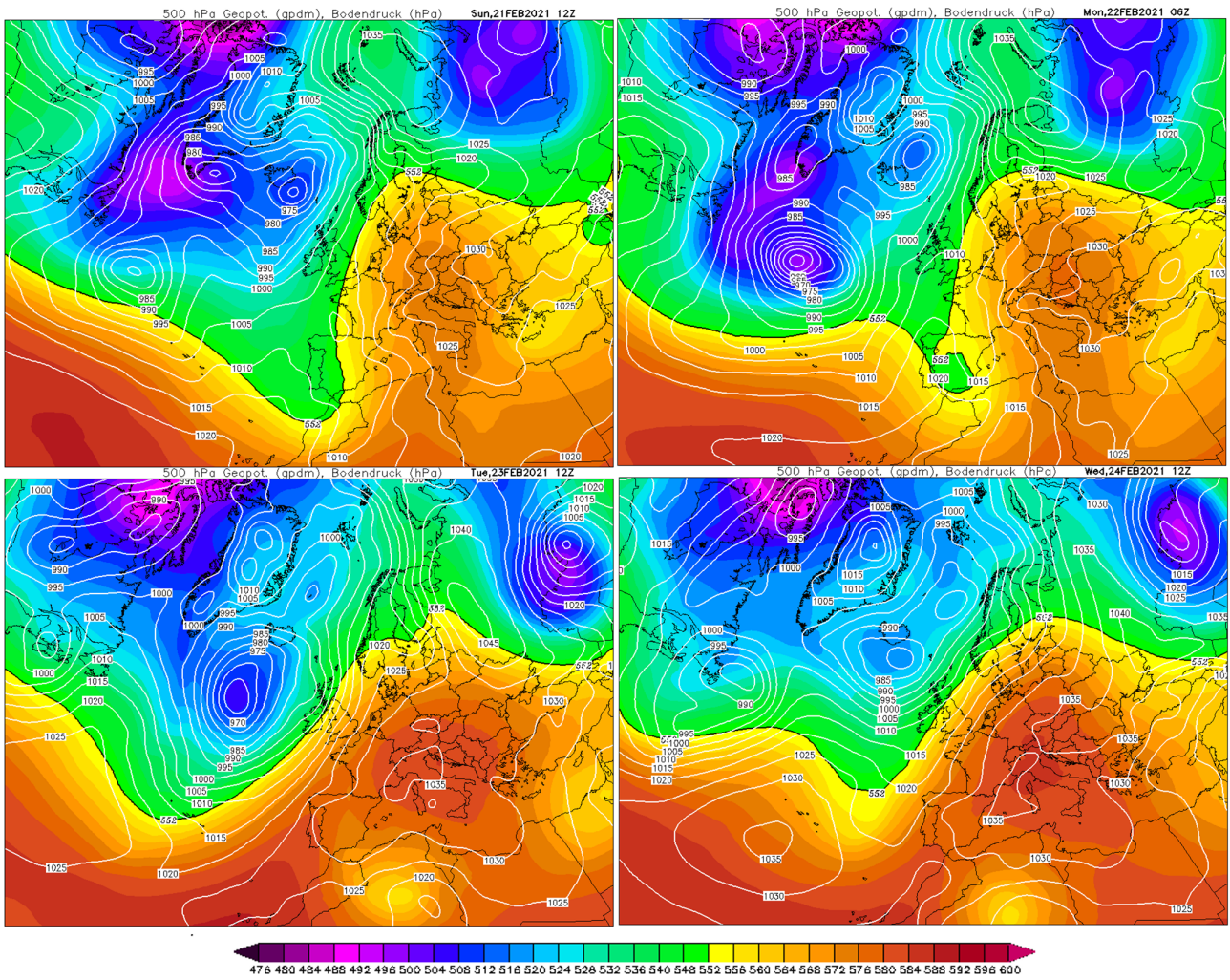


Figure 18. GFS reanalysis maps of 500 hPa geopotential (color shading) and surface pressure (white isolines) fields, for 21 February 2021 at 12 UTC, 22 February 2021 at 06 UTC, and 23 and 24 February 2021 at 12 UTC. (maps from: <https://www.wetterzentrale.de/en/reanalysis.php?model=cfsr>, accessed on 27 November 2024).

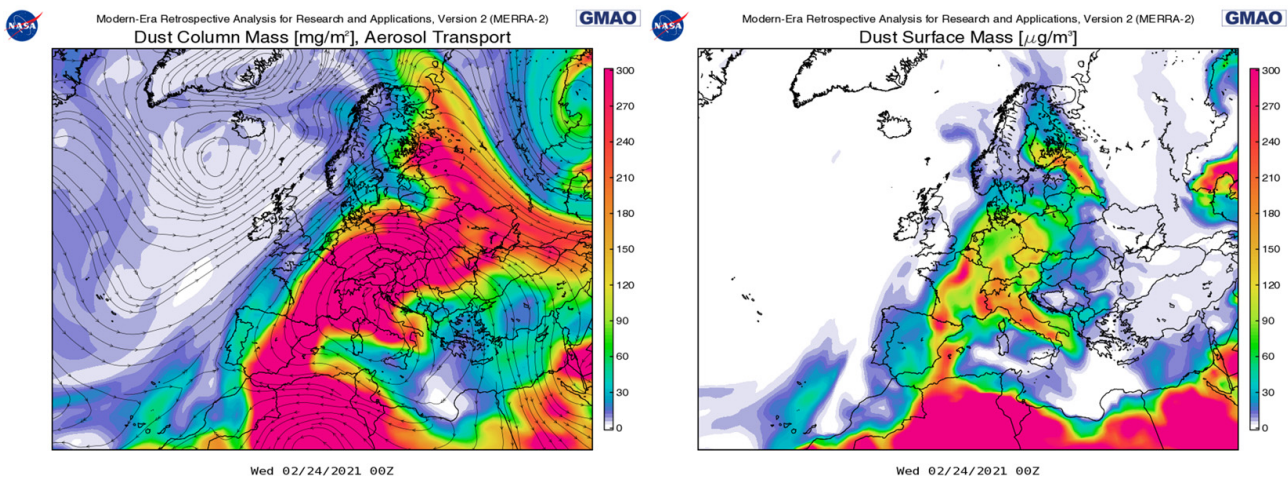


Figure 19. MERRA 2 dust column mass (left) and dust surface mass (right) maps for 24 February 2021, at 00 UTC.

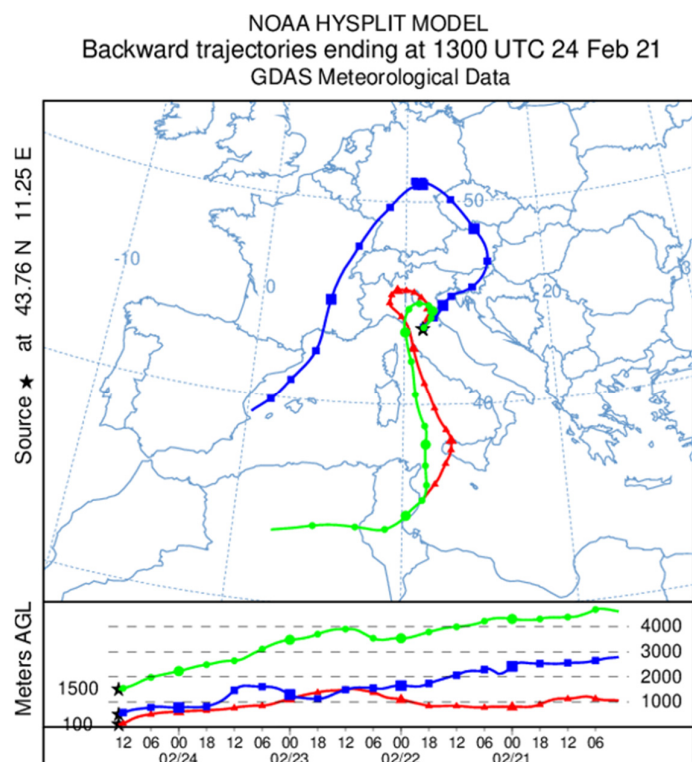


Figure 20. NOAA HYSPLIT back-trajectories estimated for 24 February 2021, at 13 UTC. The lines represent the trajectories of a particle starting at different altitudes (100, 500, and 1500 m for the red, blue, and green lines, respectively). The bottom panel shows the altitude of the particles over time.

4. Conclusions

The meteorological configurations that determine the occurrence of desert intrusions over the MB, and in particular Italy, can vary considerably, both in terms of the source areas and the trajectories that the mineral dust takes. Focusing on Saharan dust, which is the most prevalent in the study area, the meteorological patterns that favor the transport can be distinguished by south and southwest flows (“direct” case) or by longer trajectories from different directions (west and northwest, “non-direct” case). Consequently, the identification of desert episodes can be challenging, as the data obtained from local variables, such as wind and atmospheric pressure, may be inadequate to describe the meteorological dynamics that have developed over several days across a vast area, including the MB and source areas.

This work proposed an approach for the analysis of a multi-year dataset of desert episodes affecting central Italy, in order to highlight their frequency of occurrence on a seasonal basis, and their interannual variability. Additionally, a first attempt at a meteorological classification of desert intrusions was presented, using the PCT09 classification.

The method for identifying desert episodes adopted, based on a hybrid approach which exploits both the numerical forecast model data and the PM_{10} observed data, was also evaluated on the basis of false and missed alarms. In particular, false alarms, which in 70 per cent of cases occur in the days before or after dust days, can, therefore, provide information in relation to the transport phase without dust deposition, increasing knowledge of the various phases of desert intrusions.

The analysis of the dataset of desert episodes showed that dust days occur more frequently in spring and summer, in correspondence with anticyclonic conditions associated with a low baric gradient and weak winds (prevailing class CT8). Conversely, the days classified as false alarms are mainly related to classes characterized by winds from the south, west, and from north–west, compatible with transport conditions without dust

deposition (classes CT4 and CT7, respectively). Such circulation patterns mainly occur during the warm semester, but also in winter, albeit with less recurrence.

This significant frequency of ‘non-direct’ desert episodes has prompted the study of some particularly interesting cases related to the omega configuration. In fact, the latter represents a blocking condition, more frequent in February and March, which is increasing in frequency and duration as a result of climate change. Of the three case studies described in detail, the first represents the more recurrent ‘direct’ configuration, while the other two ‘non-direct’ cases concern this specific configuration, in February 2019 and 2021.

As for missed alerts, these account for about 10 per cent of the desert episodes, and are characterized by anticyclonic conditions, particularly with a high frequency of occurrence of class CT3. Looking ahead, more than one forecasting model should be used to reduce the number of missed alerts, to improve the method of selecting dust days.

Regarding the classification of the meteorological conditions favorable to desert intrusions, the application of the PCT09 classification, while revealing interesting results, is nevertheless a limited approach. In fact, this classification was not created specifically with the aim of identifying the circulations that favor dust deposition, but is limited to providing information on the day itself, without taking into account the processes that occurred on previous days at a large scale. Moreover, the domain used for the PCT09 classification includes the entire Italian territory, but does not extend to the MB and source areas. Therefore, in order to analyze the entire process that determines desert intrusions, it would be necessary to develop a specific classification that takes into account both a broader domain comprising the source areas and the patterns that develop in the days preceding dust deposition.

On the other hand, a specific classification of the various types of meteorological structures conducive to desert intrusions, applied to a multi-year dataset, can help not only to better understand the phenomenon in all its aspects, but also to understand variations in the frequency and intensity of episodes occurring in relation to particular patterns.

In the context of ongoing climate change, the implementation of appropriate classification schemes of circulation types could indeed highlight how these changes impact the dynamics of desert dust intrusions. In relation to this, the CORDEX [43] could offer a basic framework.

Supplementary Materials: The following supporting information can be downloaded at <https://www.mdpi.com/article/10.3390/air2040026/s1>, Figure S1: Seasonality frequency of PCT classes for false alarms; Figure S2: Seasonality frequency of PCT classes for missed alarms; Table S1: Table of seasonality frequency of PCT classes for dust days, false and missed alarms.

Author Contributions: F.C., A.O. and G.M. wrote the main manuscript text and prepared figures; all authors reviewed the manuscript; F.C. main data processing; A.O. and G.M. data results checks and meteorological configurations description. All authors have read and agreed to the published version of the manuscript.

Funding: This research received no external funding.

Institutional Review Board Statement: Not applicable.

Informed Consent Statement: Not applicable.

Data Availability Statement: All relevant data have been included in this paper in the form of tables and figures and in the “Supplementary Materials” section. The model simulation data and the observations data used in this study are available at the links provided in the article. Specific data requests can be addressed by e-mail to the corresponding author.

Conflicts of Interest: The authors declare no conflicts of interest.

References

1. Ginoux, P.; Chin, M.; Tegen, I.; Prospero, J.M.; Holben, B.; Dubovik, O.; Lin, S.-J. Sources and distributions of dust aerosols simulated with the GOCART model. *J. Geophys. Res. Atmos.* **2001**, *106*, 20255–20273. [[CrossRef](#)]
2. Ginoux, P.; Prospero, J.M.; Gill, T.E.; Hsu, N.C.; Zhao, M. Global-scale attribution of anthropogenic and natural dust sources and their emission rates based on MODIS Deep Blue aerosol products. *Rev. Geophys.* **2012**, *50*, 388. [[CrossRef](#)]
3. Kinne, S.; Schulz, M.; Textor, C.; Guibert, S.; Balkanski, Y.; Bauer, S.E.; Berntsen, T.; Berglen, T.F.; Boucher, O.; Chin, M.; et al. An AeroCom initial assessment—Optical properties in aerosol component modules of global models. *Atmos. Chem. Phys.* **2006**, *6*, 1815–1834. [[CrossRef](#)]
4. Wu, M.; Liu, X.; Yu, H.; Wang, H.; Shi, Y.; Yang, K.; Darmenov, A.; Wu, C.; Wang, Z.; Luo, T.; et al. Understanding processes that control dust spatial distributions with global climate models and satellite observations. *Atmos. Chem. Phys.* **2020**, *20*, 13835–13855. [[CrossRef](#)]
5. Fan, J.; Wang, Y.; Rosenfeld, D.; Liu, X. Review of Aerosol–Cloud Interactions: Mechanisms, Significance, and Challenges. *J. Atmos. Sci.* **2016**, *73*, 4221–4252. [[CrossRef](#)]
6. Li, X.; Zhang, Q.; Xue, H. The role of initial cloud condensation nuclei concentration in hail using the WRF NSSL 2-moment microphysics scheme. *Adv. Atmos. Sci.* **2017**, *34*, 1106–1120. [[CrossRef](#)]
7. Rosenfeld, D.; Zhu, Y.; Wang, M.; Zheng, D.Y.; Goren, T.; Yu, S. Aerosol-driven droplet concentrations dominate coverage and water of oceanic low-level clouds. *Science* **2019**, *363*, eaav0566. [[CrossRef](#)]
8. Portner, H.-O.; Roberts, D.C.; Tignor, M.; Poloczanska, E.S.; Mintenbeck, K.; Alegria, A.; Craig, M.; Langsdorf, S.; Loschke, S.; Moller, V.; et al. (Eds.) IPCC, 2022: Climate Change, 2022. Impacts, Adaptation, and Vulnerability. In *Contribution of Working Group II to the Sixth Assessment Report of the Intergovernmental Panel on Climate Change*; Cambridge University Press: Cambridge, UK; New York, NY, USA, 2022; p. 3056. [[CrossRef](#)]
9. Mahowald, N.M.; Li, L.; Albani, S.; Hamilton, D.S.; Kok, J.F. The importance of historical and paleoclimate aerosol radiative effects. *Atmos. Chem. Phys.* **2024**, *24*, 533–551. [[CrossRef](#)]
10. Skeie, R.B.; Aldrin, M.; Berntsen, T.K.; Holden, M.; Huseby, R.B.; Myhre, G.; Storelvmo, T. The aerosol pathway is crucial for observationally constrained climate sensitivity and anthropogenic forcing. *EGU Sphere* **2024**, *15*, 1435–1458. [[CrossRef](#)]
11. Jickells, T.D.; Anderson, K.; Andersen, K.K.; Baker, A.R.; Bergametti, G.; Brooks, N.; Cao, J.J.; Boyd, P.W.; Duce, R.A.; Hunter, K.A.; et al. Global Iron Connections between Desert Dust. *Ocean Biogeochem. Climate Sci.* **2005**, *308*, 67–71.
12. Ravelo-Pérez, L.M.; Rodríguez, S.; Galindo, L.; García, M.I.; Alastuey, A.; López-Solano, J. Soluble iron dust export in the high altitude Saharan Air Layer. *Atmos. Environ.* **2016**, *133*, 49–59. [[CrossRef](#)]
13. Prospero, J.M.; Ginoux, P.; Torres, O.; Nicholson, S.E.; Gill, T.E. Environmental characterization of global sources of atmospheric soil dust identified with the nimbus 7 total ozone mappingspectrometer (TOMS) absorbing aerosol product. *Rev. Geophys.* **2002**, *40*, 1002. [[CrossRef](#)]
14. Goudie, A.S.; Middleton, N.J. *Desert Dust in the Global System*; Springer: Berlin/Heidelberg, Germany; New York, NY, USA, 2006; ISBN 3-540-32354-6.
15. Gavrouzou, M.; Hatzianastassiou, N.; Gkikas, A.; Korras-Carraca, M.-B.; Mihalopoulos, N. A Global Climatology of Dust Aerosols Based on Satellite Data: Spatial, Seasonal and Inter-Annual Patterns over the Period 2005–2019. *Remote Sens.* **2021**, *13*, 359. [[CrossRef](#)]
16. Bullard, J.E.; Baddock, M.; Bradwell, T.; Crusius, J.; Darlington, E.; Gaiero, D.; Gassó, S.; Gísladóttir, G.; Hodgkins, R.; McCulloch, R.; et al. High-latitude dust in the Earth system. *Rev. Geophys.* **2016**, *54*, 447–485. [[CrossRef](#)]
17. Meinander, O.; Dagsson-Waldhauserova, P.; Amosov, P.; Aseyeva, E.; Atkins, C.; Baklanov, A.; Baldo, C.; Barr, S.L.; Barzycka, B.; Benning, L.G.; et al. Newly identified climatically and environmentally significant high-latitude dust sources. *Atmos. Chem. Phys.* **2022**, *22*, 11889–11930. [[CrossRef](#)]
18. Alastuey, A.; Querol, X.; Aas, W.; Lucarelli, F.; Pérez, N.; Moreno, T.; Cavalli, F.; Areskou, H.; Balan, V.; Catrambone, M.; et al. Geochemistry of PM₁₀ over Europe during the EMEP intensive measurement periods in summer 2012 and winter 2013. *Atm. Chem. Phys.* **2016**, *16*, 6107–6129. [[CrossRef](#)]
19. Rodríguez, S.; Calzolari, G.; Chiari, M.; Nava, S.; García, M.I.; López-Solano, J.; Marrero, C.; López-Darias, J.; Cuevas, E.; Alonso-Pérez, S.; et al. Rapid changes of dust geochemistry in the Saharan Air Layer linked to sources and meteorology. *Atmos. Environ.* **2020**, *223*, 117186. [[CrossRef](#)]
20. Stafoggia, M.; Zauli-Sajani, S.; Pey, J.; Samoli, E.; Alessandrini, E.; Basagaña, X.; Cernigliaro, A.; Chiusolo, M.; Demaria, M.; Díaz, J.; et al. Desert Dust Outbreaks in Southern Europe: Contribution to Daily PM₁₀ Concentrations and Short-Term Associations with Mortality and Hospital Admissions. *Environ. Health Perspect.* **2016**, *124*, 413–419. [[CrossRef](#)] [[PubMed](#)] [[PubMed Central](#)]
21. Domínguez-Rodríguez, A.; Báez-Ferrer, N.; Abreu-González, P.; Rodríguez, S.; Díaz, R.; Avanzas, P.; Hernández-Vaquero, D. Impact of Desert Dust Events on the Cardiovascular Disease: A Systematic Review and Meta-Analysis. *J. Clin. Med.* **2021**, *10*, 727. [[CrossRef](#)]
22. Karanasiou, A.; Moreno, N.; Moreno, T.; Viana, M.; De Leeuw, F.; Querol, X. Health effects from Sahara dust episodes in Europe: Literature review and research gaps. *Environ. Int.* **2012**, *47*, 107–114. [[CrossRef](#)] [[PubMed](#)]
23. Kotsyfakis, M.; Zargiannis, S.G.; Patelarou, E. The health impact of Saharan dust exposure. *Int. J. Occup. Med. Environ. Health* **2019**, *32*, 749–760. [[CrossRef](#)] [[PubMed](#)]

24. Harr, B.; Pu, B.; Jin, Q. The Emission, Transport, and Impacts of the Extreme Saharan Dust Storm in 2015. *EGUsphere* **2024**, *24*, 8625–8651. [[CrossRef](#)]
25. Van der Does, M.; Brummer, G.-J.A.; Korte, L.F.; Stuut, J.-B.W. Seasonality in Saharan dust across the Atlantic Ocean: From atmospheric transport to seafloor deposition. *J. Geophys. Res. Atmos.* **2021**, *126*, e2021JD034614. [[CrossRef](#)]
26. Francis, D.; Nelli, N.; Fonseca, R.; Weston, M.; Flamant, C.; Cherif, C. The dust load and radiative impact associated with the June 2020 historical Saharan dust storm. *Atmos. Environ.* **2022**, *268*, 118808. [[CrossRef](#)]
27. Gavrouzou, M.; Hatzianastassiou, N.; Gkikas, A.; Lolis, C.J.; Mihalopoulos, N. A Climatological Assessment of Intense Desert Dust Episodes over the Broader Mediterranean Basin Based on Satellite Data. *Remote Sens.* **2021**, *13*, 2895. [[CrossRef](#)]
28. EU-Dir. Directive 2008/50/EC of the European Parliament and of the Council of 21 May 2008 on Ambient Air Quality and Cleaner Air for Europe. *Official Journal of the European Union*. 2008. Available online: <http://data.europa.eu/eli/dir/2008/50/oj> (accessed on 27 November 2024).
29. EU-SEC. Establishing Guidelines for Demonstration and Subtraction of Exceedances Attributable to Natural Sources Under the Directive 2008/50/EC on Ambient Air Quality and Cleaner Air for Europe. 2011. Available online: <https://data.consilium.europa.eu/doc/document/ST%206771%202011%20INIT/EN/pdf> (accessed on 27 November 2024).
30. Escudero, M.; Querol, X.; Pey, J.; Alastuey, A.; Pérez, N.; Ferreira, F.; Alonso, S.; Rodríguez, S.; Cuevas, E. A methodology for the quantification of the net African dust load in air quality monitoring networks. *Atmos. Environ.* **2007**, *41*, 5516–5524. [[CrossRef](#)]
31. Barnaba, F.; Bolignano, A.; Di Liberto, L.; Morelli, M.; Lucarelli, F.; Nava, S.; Perrino, C.; Canepari, S.; Basart, S.; Costabile, F.; et al. Desert dust contribution to PM₁₀ loads in Italy: Methods and recommendations addressing the relevant European Commission Guidelines in support to the Air Quality Directive 2008/50. *Atmos. Environ.* **2017**, *161*, 288–305. [[CrossRef](#)]
32. Gobbi, G.P.; Barnaba, F.; Di Liberto, L.; Bolignano, A.; Lucarelli, F.; Nava, S.; Perrino, C.; Pietrodangelo, A.; Basart, S.; Costabile, F.; et al. An inclusive view of Saharan dust advections to Italy and the Central Mediterranean. *Atmos. Environ.* **2019**, *201*, 242–256. [[CrossRef](#)]
33. Barnaba, F.; Alvan Romero, N.; Bolignano, A.; Basart, S.; Renzi, M.; Stafoggia, M. Multiannual assessment of the desert dust impact on air quality in Italy combining PM₁₀ data with physics-based and geostatistical models. *Environ. Int.* **2022**, *163*, 107204. [[CrossRef](#)]
34. Tositti, L.; Brattich, E.; Cassardo, C.; Morozzi, P.; Bracci, A.; Marinoni, A.; Di Sabatino, S.; Porcù, F.; Zappi, A. Development and evolution of an anomalous Asian dust event across Europe in March 2020. *Atmos. Chem. Phys.* **2022**, *22*, 4047–4073. [[CrossRef](#)]
35. Mifka, B.; Telišman Prtenjak, M.; Kavre Piltaver, I.; Mekterović, D.; Kuzmić, J.; Marciuš, M.; Ciglencečki, I. Intense desert dust event in the northern Adriatic (March 2020); insights from the numerical model application and chemical characterization results. *Earth Space Sci.* **2023**, *10*, e2023EA002879. [[CrossRef](#)]
36. Salvador, P.; Pey, J.; Pérez, N.; Querol, X.; Artiñano, B. Increasing atmospheric dust transport towards the western Mediterranean over 1948–2020. *npj Clim Atmos Sci.* **2022**, *5*, 34. [[CrossRef](#)]
37. Cuevas-Agulló, E.; Barriopedro, D.; García, R.D.; AlonsoPérez, S.; González-Alemán, J.J.; Werner, E.; Suárez, D.; Bustos, J.J.; García-Castrillo, G.; García, O.; et al. Sharp increase in Saharan dust intrusions over the western Euro-Mediterranean in February–March 2020–2022 and associated atmospheric circulation. *Atmos. Chem. Phys.* **2024**, *24*, 4083–4104. [[CrossRef](#)]
38. Fabiano, F.; Meccia, V.L.; Davini, P.; Ghinassi, P.; Corti, S. A regime view of future atmospheric circulation changes in northern mid-latitudes. *Weather Clim. Dyn.* **2021**, *2*, 163–180. [[CrossRef](#)]
39. Lakson, M.; Post, P.; Sepp, M. The Impact of Atmospheric Circulation on Air Temperature Rise in Estonia. *Front. Earth Sci.* **2019**, *7*, 131. [[CrossRef](#)]
40. Huth, R. A circulation classification scheme applicable in GCM Studies. *Theor. Appl. Climatol.* **2000**, *67*, 1–18. [[CrossRef](#)]
41. Iannuccilli, M.; Bartolini, G.; Betti, G.; Crisci, A.; Grifoni, D.; Gozzini, B.; Messeri, A.; Morabito, M.; Tei, C.; Torrigiani Malaspina, T.; et al. Extreme precipitation events and their relationships with circulation types in Italy. *Int. J. Clim.* **2021**, *41*, 4769–4793. [[CrossRef](#)]
42. Detring, C.; Müller, A.; Schielicke, L.; Névir, P.; Rust, H.W. Occurrence and transition probabilities of omega and high-over-low blocking in the Euro-Atlantic region. *Weather Clim. Dyn.* **2021**, *2*, 927–952. [[CrossRef](#)]
43. Vautard, R.; Kadyrov, N.; Iles, C.; Boberg, F.; Buonomo, E.; Bülow, K.; Coppola, E.; Corre, L.; Van Meijgaard, E.; Nogherotto, R.; et al. Evaluation of the Large EURO-CORDEX Regional Climate Model Ensemble. *J. Geophys. Res. Atmos.* **2021**, *126*, e2019JD032344. [[CrossRef](#)]

Disclaimer/Publisher’s Note: The statements, opinions and data contained in all publications are solely those of the individual author(s) and contributor(s) and not of MDPI and/or the editor(s). MDPI and/or the editor(s) disclaim responsibility for any injury to people or property resulting from any ideas, methods, instructions or products referred to in the content.